Electron density and temperature measurements in a magnetized expanding hydrogen plasma

R. Leyte-González,* J. M. Palomares, D. C. Schram, and R. Engeln
Department of Applied Physics, Eindhoven University of Technology, De Zaale, 5612 AJ Eindhoven, The Netherlands
(Received 16 November 2015; revised manuscript received 2 June 2016; published 1 August 2016)

We report measurements of electron densities, n_e, and temperatures, T_e, in a magnetized expanding hydrogen plasma performed using Thomson scattering. The effects of applying an axial magnetic field and changing the background pressure in the plasma vessel on n_e and T_e along the expansion axis are reported. Magnetic field strengths (B field) up to 170 mT were applied, which are one order of magnitude larger than previously reported. The main effect of the applied B field is the plasma confinement, which leads to higher n_e. At B fields larger than 88 mT the electron density along the expansion axis does not depend strongly on the magnetic field strength. However, T_e is susceptible to the B field and reaches at 170 mT a maximum of 2.5 eV at a distance of 1.5 cm from the exit of the cascaded arc. To determine also the effect of the arc current through the arc, measurements were performed with arc currents of 45, 60, and 75 A at background pressures of 9.7 and 88.3 Pa. At constant magnetic field n_e decreases from the exit of the arc along the expansion axis when the arc current is decreased. At 88.3 Pa n_e shows a higher value close to the exit of the arc, but a faster decay along the expansion axis with respect to the 9.7 Pa case. T_e is overall higher at lower pressure reaching a maximum of 3.2 eV at the lower arc current of 45 A. The results of this study complement our understanding and the characterization of expanding hydrogen plasmas.

DOI: 10.1103/PhysRevE.94.023201

I. INTRODUCTION

From a fundamental point of view and due to its potential applications, expanding plasmas are a topic of extensive research [1–7]. These plasmas can be produced by a cascaded arc [8] and are sources of different particles such as electrons, positive and negative ions, radicals, and neutral atoms [9]. van de Sanden *et al.* studied the fundamental properties of Ar expanding plasmas at low pressures (13–133 Pa) for magnetized and nonmagnetized cases [2,3]. Mazouffre *et al.* focused on the transport phenomena of Ar-H_2 mixture plasmas [5]. A particular case is that of the expanding pure hydrogen plasmas on which de Graaf [10] and Vankan *et al.* [6] investigated the influence of rovibrational excited hydrogen molecules on the plasma kinetics.

Low pressure magnetized expanding plasmas are suitable to study the effects of particle fluxes on materials. The effect of the applied B field is the confinement of the plasma, which leads to higher n_e. Several linear plasma devices have been used for this purpose, e.g., PISCES [11] and NAGDIS [12], characterizing the plasmas in terms of electron density and temperature. In [11,12] electron densities in magnetized hydrogen plasmas are reported of, respectively, 1×10^{19} and 2.4×10^{19} m^{-3} using B fields in the range between 200 and 400 mT. Regarding the electron temperature, in PISCES this is between 5 and 7 eV and in NAGDIS around 6.0 eV. Thomson scattering measurements on magnetized expanding hydrogen plasmas for fusion-related purposes have been carried out by van der Meiden *et al.* [13] using magnetic fields between 400 mT and 1.6 T and a background pressure of about 1 Pa. They reported electron densities on the order of a few times 10^{20} m^{-3}. Vijvers *et al.* [14] have performed Thomson scattering on magnetized hydrogen plasmas measuring n_e up to 9×10^{21} m^{-3} with a magnetic field of 200 mT. Research conducted by van Rooij *et al.* [15] employing hydrogen in a linear plasma device, called Pilot-PSI, working with a maximum magnetic field of 1.6 T and background pressures of 0.2–2 Pa. They reported electron densities of 5×10^{21} m^{-3} and electron temperatures up to 3.0 eV. De Temmerman *et al.* [16], utilizing another linear plasma reactor (Magnum-PSI), studied the effect of the presence of negative hydrogen ions in a magnetized plasma expansion on the etching of surfaces. At the current status of Magnum-PSI electron densities up to 7×10^{20} m^{-3} and maximum temperatures of 3.5 eV were measured in hydrogen for a B field of 1.7 T.

Another example is the study carried out by van Harskamp *et al.* [9] dealing with fundamental reaction processes such as population inversion in a magnetized expanding hydrogen plasma using a magnetic field of 14 mT and background pressure of 9 Pa.

The goal of our work is to get insight into the reaction mechanisms in expanding thermal plasmas in a range of magnetic fields not covered in previous studies. We report on the effect of the magnetic field on n_e and T_e in particular in the range of magnetic fields between 88 and 170 mT (applied parallel to the z axis). The effect of background pressure and arc current on n_e and T_e in the plasma expansion is also reported. A maximum n_e of about 3×10^{20} m^{-3} was measured for $B = 170$ mT at a distance of 1.5 cm from the exit of the source. We found that at constant magnetic field n_e decreases from the exit of the arc along the expansion axis when the arc current is decreased. It was observed that at B fields larger than 88 mT the electron density along the expansion axis does not depend strongly on the magnetic field strength. However, T_e is susceptible to the B field and reaches at 170 mT a maximum of 2.5 eV at $z = 1.5$. For a pressure of 88.3 Pa the electron density shows, compared to a pressure of 9.7 Pa, a higher value close to the exit of the arc, but decays faster along the expansion axis. T_e is overall higher at lower pressure.

Our measurements are performed along the plasma beam (z direction), which can be performed because our plasma source can be moved with respect to the excitation and detection volume. In most linear plasma devices, measurements can

*r.leyte.gonzalez@tue.nl

only be performed at discrete positions on the expansion axis. This study complements the characterization of these types of expanding hydrogen plasmas.

II. EXPERIMENTAL SETUP

To measure n_e and T_e in the plasma expansion a Thomson scattering laser system was tailor built (described in detail in the Sec. II B) on our linear plasma device, called PLEXIS. A unique feature of PLEXIS is the movable arm on which the arc is mounted (*vide infra*); it allows measuring n_e and T_e in the plasma expansion as a function of the distance from the exit of the source without changing the alignment of the excitation and detection volume. A description of the plasma reactor and the cascaded arc plasma source are given in the following sections.

A. Plasma source and reactor

The measurements were carried out in the linear plasma device PLEXIS (plasma expanding in interaction with surfaces) shown schematically in Fig. 1. This device consists of a cascaded arc plasma source [1] within a stainless steel vessel, which has several observation ports for diagnostics. The cascaded arc was developed by Maecker [8] and its working principle has been treated in detail by, e.g., Kroesen *et al.* [1], de Graaf *et al.* [10], and van de Sanden *et al.* [2], among others. The cascaded arc is mounted on a movable arm, allowing a change of the position in three dimensions. This has the advantage that measurements can be performed at almost any position in the expanding plasma. The plasma is ignited by three tungsten-lanthanum cathodes and is contained within the bore of the cascaded arc formed by four water-cooled copper plates separated and insulated by polyvinyl chloride (PVC) spacers. Each copper plate has a centered circular aperture of 4 mm diameter. When stacked the four copper plates together form the plasma channel.

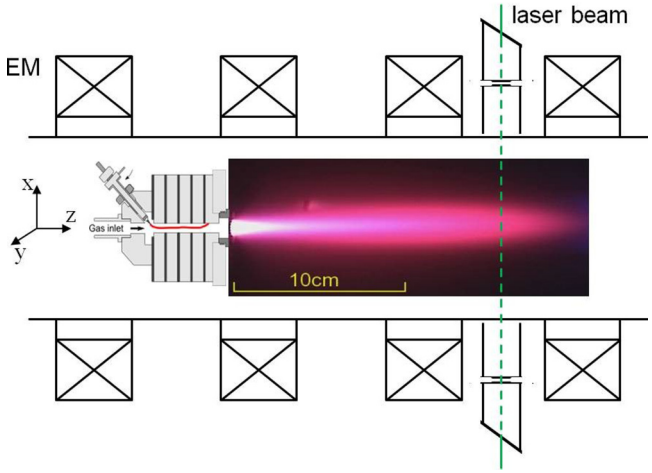

FIG. 1. Schematic representation of the linear plasma device PLEXIS. It shows the movable cascaded arc plasma source, the confined hydrogen plasma, and the Nd:YAG laser beam path, across the plasma (not to scale). The four copper coils produce the magnetic field along the z axis.

At the end of the cascaded arc a 7.2-mm-long nozzle is mounted, which acts as an anode. The inner diameter of this nozzle is 9.6 mm, which leads to higher values of electron densities as compared to a nozzle with a 4.0 mm diameter, i.e., the same as the diameter of the bore of the arc. That the shape of the nozzle has a strong effect on the amount of charged and excited particles in the hydrogen expanding plasma was studied by Vankan *et al.* [17] and Gabriel *et al.* [18]. The losses of H^+, H atoms and electrons occurs through molecular assisted recombination processes (MAR) in the nozzle and the formation of rotationally and vibrationally excited hydrogen (H_2^{rv}) molecules at the surface of the nozzle.

The hydrogen flow through the bore of the arc is kept at 3000 standard cubic centimeters per minute (sccm). Two background pressures (p_{BG}) were used in the reactor: 9.7 and 88.3 Pa. The total arc current (I_{arc}) through the three cathodes was 45, 60, and 75 A, resulting in input powers of 7.1, 8.7, and 10.3 kW, respectively.

The magnetic field is produced and controlled by four Helmholtz electromagnets mounted around the vessel. The setup allows changing the magnetic field strength from 10 mT up to a maximum of 170 mT. The magnetic field strength was controlled by means of the current through the four copper coils (EM) which can generate a uniform axial field over a length of about 1.5 m. For the highest magnetic field of 170 mT (400 A through the coils), the current can only be applied during 1 min, because of the heating of the coils. The experiments have been performed with magnetic field strengths of 88, 140, and 170 mT. The cascaded arc plasma source can be displaced within the reactor along the three axes. The direction of the main expansion of the plasma is taken as the z axis; see Fig. 1. The reference initial position along the z axis is described in the next section.

B. Thomson scattering diagnostic

The source of laser light for the Thomson scattering setup (Fig. 2) is a Nd:YAG laser (GCR 3 Quanta Ray) operating at the second harmonic ($\lambda = 532.1$ nm, $E_{pulse} = 0.5$ J, $f_{rep} = 10$ Hz,

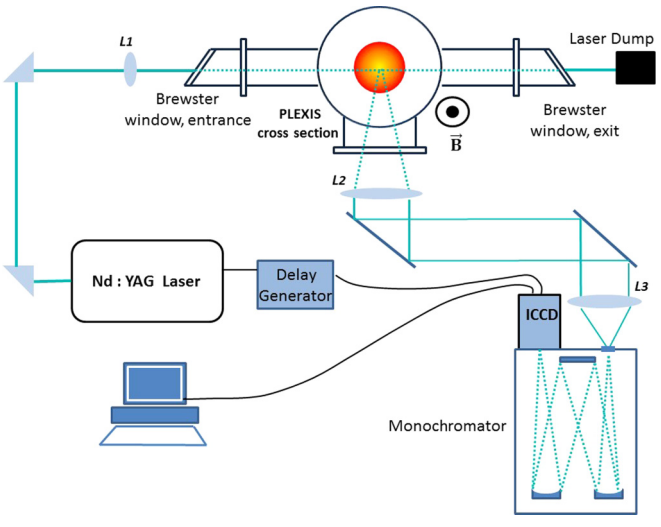

FIG. 2. Schematic representation of the Thomson scattering laser system built on PLEXIS (components are not to scale).

$t_{pulse} = 9$ ns). Three 90° prisms and a lens L1($f = 1000$ mm) guide and focus the laser beam into the vessel. The scattering volume is determined by the laser focus and the collection optics, and is about 17.0 mm with a spot size of about 0.1 mm. The laser light is polarized perpendicular to the direction of the collected signal. Lens L1 is antireflection coated for 532 nm, to minimize laser beam power losses. In order to reduce the stray light inside the vacuum chamber, two quartz windows are mounted at the Brewster angle at the entrance and exit of the beam path. Additionally, two diaphragms are placed inside the entrance and exit tubes at a distance of 22 cm from the center of the vessel. This type of arrangement was used by van der Meiden *et al.* [19], achieving a considerable decrease of the stray light.

C. Detection system

The scattered light is collected perpendicular to both the laser beam and plasma beam, and guided by two plano-convex lenses: L2 and L3 ($f = 500$ mm), and two flat mirrors. The lenses image the scattered light from the detection volume in a 1:1 image onto the slit (100 μm) of a monochromator (Jobin Yvon R640, Czerny-Turner configuration). The monochromator is equipped with a concave holographic grating (1200 lines/mm, and $f = 640$ mm). The signal is detected with an intensified charge-coupled device (CCD) camera i-Star 764. The photocathode of the iCCD intensifier has a quantum efficiency of 12% at 530 nm. The grating is positioned such that the CCD sensor detects light in the spectral range from 525 to 539 nm. The spectral range and resolution were calibrated using a neon lamp with emission lines at $\lambda = 533.07$ and 534.10 nm, and the laser beam at $\lambda = 532.1$ nm. A delay generator (Stanford Research Systems, Model DG535) was used to synchronize the laser pulse with the acquisition gate (50 ns) of the iCCD camera triggered by the laser Q-switch signal. The total integration time was 3 μs (600 laser shots).

III. MEASURING PROCEDURE AND DATA ANALYSIS

The signal intensities of Rayleigh and Raman scattering are used for the absolute calibration of the Thomson scattering setup. For this purpose the absolute cross sections, densities, and temperatures of two different gas samples (in this work Ar and N_2) were used. Rayleigh scattering cross sections are smaller than the Thomson scattering cross section; nevertheless, the Rayleigh scattering intensity is higher than the Thomson scattering intensity, because the neutral density is normally much higher than the electron density. The high Rayleigh scattering intensity can cause saturation of the detector, and filters have to be employed which in most of the cases reduce the accuracy of the calibration. Also, the stray light is scattered at the same wavelength as Rayleigh scattering. In order to distinguish Rayleigh scattered light from stray light, measurements at different pressures (or different gases) are needed. Raman scattering offers the advantage that the scattered signal is at different wavelengths with respect to stray light and Rayleigh scattering. Raman calibration has been used by De Regt *et al.* [20] and van Gessel *et al.* [21]; hence it represents an alternative method for the absolute calibration.

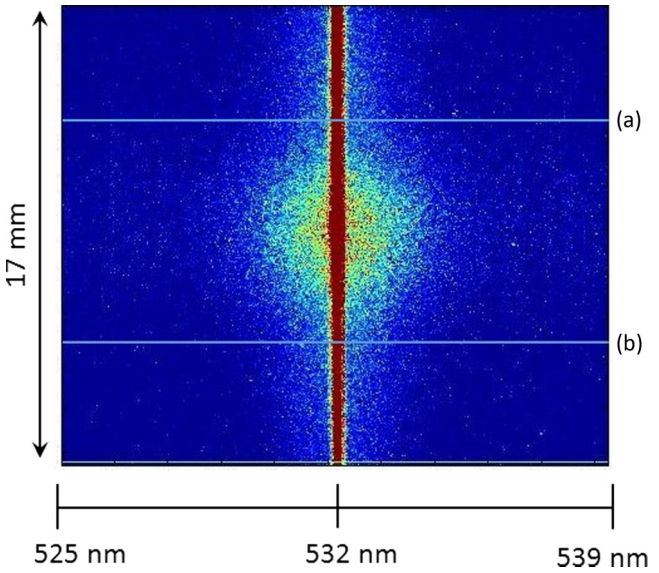

FIG. 3. iCCD image of the scattering of the Nd:YAG laser in a magnetized hydrogen plasma expansion at $z = 1.5$ cm (z axis is parallel to the wavelength axis in the plot). The region between row (a) and row (b) is divided into 17 equal sections and each section is binned along the y axis. Then the stray light subtraction, Rayleigh calibration, and Thomson fitting are performed for every section separately. The experimental conditions were H_2 flow of 3000 sccm, $p_{BG} = 88.3$ Pa, $B = 170$ mT, $I_{arc} = 45$ A, and $z = 1.5$ cm. The image is obtained by accumulating 600 laser shots.

A. Calibration

The first step in the absolute calibration of the Thomson scattering system was the determination of the stray light, which originates from the reflection of the laser light from metallic or polished surfaces such as the windows of the plasma vessel. In our setup the entrance and exit windows for the laser are attached to two long tubes and by the use of diaphragms, as indicated in Sec. III B, the amount of stay light reaching the detector is very low. And because of this very low amount of stray light, we were able to measure Thomson scattering light without the use of a triple grating spectrometer as was used in other studies [21,22].

The first position at which measurements were performed along the main expansion axis was $z = 1.5$ cm from the exit of the nozzle. Closer to the arc the light reflected from the front of the arc was so large that the Thomson scattering signal could not be distinguished from the stray light. The $z = 0$ position is the same as used by van Harskamp *et al.* [23], i.e., at the exit of the nozzle. Figure 3 shows a typical iCCD image of the laser scattering from a magnetized hydrogen plasma. The vertical axis of the iCCD image corresponds to the spatial distribution of the scattered light and the horizontal axis to the wavelength dispersion. In Fig. 3 at 532.1 nm along the laser light (in the figure from the bottom to the top), the strong and narrow Rayleigh scattering signal is observed, together with the stray light. In the center of the image the Thomson signal

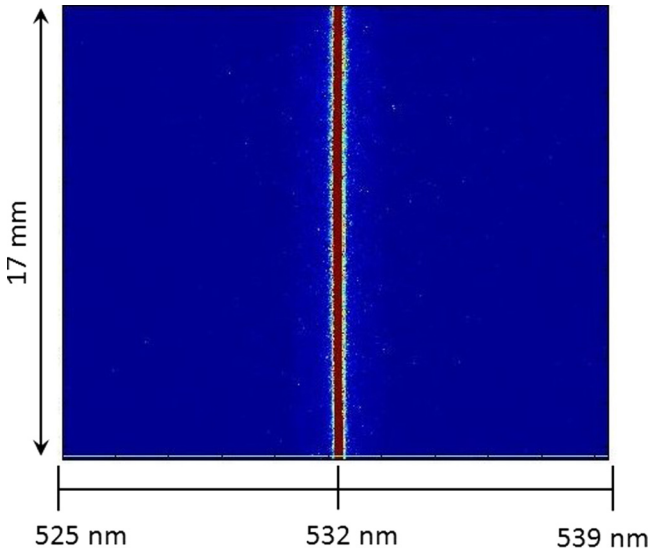

FIG. 4. Reference iCCD image of stray light and Rayleigh signals of the Nd:YAG laser beam (532 nm), in Ar gas, $p_{BG} = 72.6$ Pa. The horizontal axis corresponds to the wavelength dispersion from 525 to 539 nm (z axis is parallel to the wavelength axis in the plot) and the vertical axis corresponds to the spatial distribution of 17 mm.

is clearly visible on the left and right side of the Rayleigh scattering and stray light signal.

For each Rayleigh and Thomson scattering measurement we selected the central part of the iCCD frame (corresponding to the most intense Thomson signal), i.e., the area between row (a) and row (b) as indicated in Fig. 3. This region of the iCCD was divided into 17 equal sections and each section is binned along the y axis. Then the stray light subtraction, Rayleigh calibration, and Thomson fitting are performed for every section separately. For the reported values along the z axis we simply take the central section, which corresponds to ninth section out of the 17 sections, where the intensity is the highest.

Figure 4 shows a typical iCCD image of the Rayleigh and stray light scattering from the incoming laser in pure Ar gas at a pressure of 72.6 Pa. In order to determine the Rayleigh and stray light contributions separately, measurements of the Rayleigh and stray light signals on Ar were taken at two different pressures, 7.2 and 72.6 Pa. The Rayleigh signal was obtained from subtracting the stray light from the spectrum of the total scattering; see Fig. 5.

After obtaining the stray light as shown in Fig. 5, it can be subtracted from the measurements taken from a plasma, leaving only the Thomson and Rayleigh contributions. Thus, both Thomson and Rayleigh signals are fitted independently to Gaussian curves. Another option is to ignore the central region (Rayleigh signal) of the collected spectra and directly fit the leftover signal to the single Gaussian curve of the Thomson scattering. This is valid because the influence that Rayleigh scattering could have on the broadening of the Thomson signal is negligible, due to the fact it is very narrow (see Fig. 5).

Figure 6 shows an example of a Thomson signal obtained after removing the stray light signal and eliminating the central part of the spectrum. The Thomson scattering signal was fitted for one case of the largest alpha parameter (α) by using a

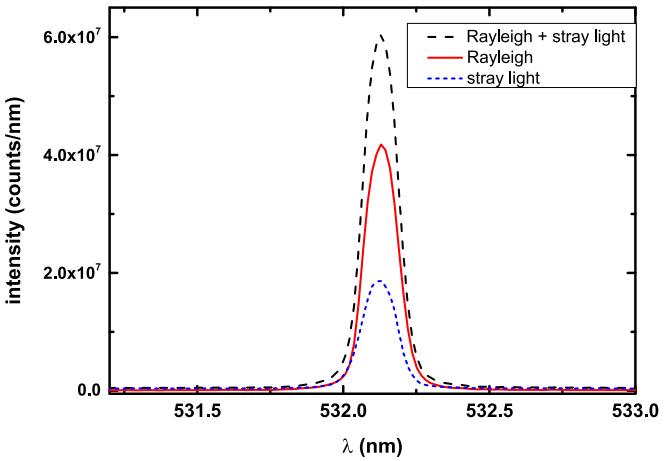

FIG. 5. Typical Rayleigh plus stray light signal (long-dashed line) of the scattered Nd:YAG laser beam at 532.1 nm in Ar, $p_{BG} = 217$ Pa, at $z = 1.5$ cm. The contribution of stray light (short-dashed line) and Rayleigh scattering (solid line) are shown separately.

Thomson scattering calculation. Under our experimental conditions the highest value for alpha was 0.088. It was found that the Thomson scattering calculation differs much less than 10% with respect to a Gaussian fit. Hence, in the analysis of our measurements we used a Gaussian fit to determine the electron density and temperature. In Fig. 6 is shown the Thomson signal fitted by a Gaussian profile, where the residue (blue line) is shown of a Gaussian fit (red line) to the Thomson signal (black line).

That we can use a Gaussian fitting for the Thomson scattering signal can also be explained as follows. The electrons in the plasma which experience the laser radiation will oscillate with the frequency of that radiation. This oscillation will generate dipole radiation in all directions (except the dipole axis), at the

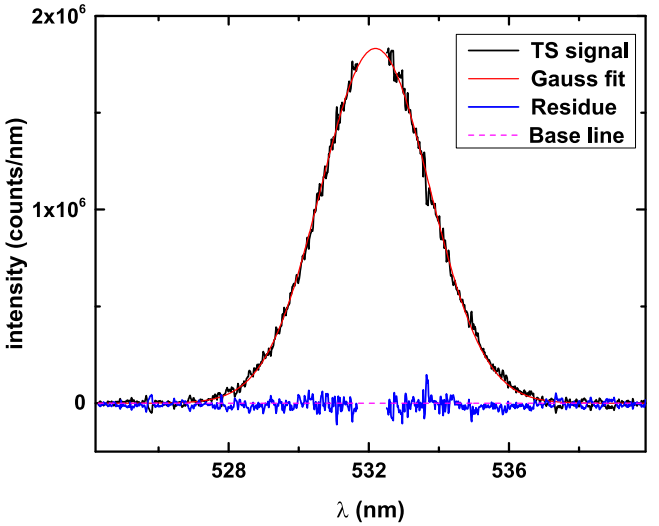

FIG. 6. Thomson scattering signal (black line) integrated over 600 laser shots. H_2 flow of 3000 sccm, $p_{BG} = 88.3$ Pa, 170 mT, 75 A, at $z = 1.5$ cm. Rayleigh signal was removed (central part of the spectrum). In red is the Gaussian fit, from which the n_e and T_e values were obtained. The blue line along the baseline (dashed line) shows the residue.

same wavelength of the laser radiation, but Doppler broadened due to the movement of the electrons. This Thomson scattering can be treated as incoherent if the scattering parameter, α, is less than 1. As will be shown later, the values of n_e and T_e reported in this paper are in the range of, respectively, $1.7 \times 10^{19} - 3 \times 10^{20}\,\mathrm{m}^{-3}$ and 0.5–2.5 eV. In that case α is between 0.052 and 0.088. Therefore, having incoherent Thomson scattering and Maxwellian velocity distributions, this leads to Gaussian scattering profiles centered at the laser wavelength. This has also been a standard procedure in similar works [2,21,24].

Inverse bremsstrahlung, i.e., electron heating due to the absorption of photons, needs to be considered. The laser produces light pulses with an energy of 500 mJ/pulse at 10 Hz repetition rate. The laser beam is focused to a spot with an area of $1.1 \times 10^{-6}\,\mathrm{m}^2$. This leads to a power density in the focus of the laser beam of $45.4\,\mathrm{GW/cm}^2$. Under the assumption that the heat is not dissipated during the laser pulse (9 ns), the increase of T_e can be calculated as shown by Kunze [25]. Using $T_e = 2.5$ eV where n_e is the highest, where the probability of photoabsorption is maximal, the expected increase of T_e is about 0.2%. Therefore the induced electron heating by inverse bremsstrahlung can be neglected.

The experimental setup was calibrated in order to get absolute values of the local electron densities from the Thomson scattering signal. For any linear scattering mechanism the scattered power P (or intensity) is linearly proportional to the incident laser power P_i, the differential cross section $d\sigma/d\Omega$, the detection length over which the scattering is collected, and the density of the scattering particles n. Two methods were used for the calibration, one based on Rayleigh scattering and one on Raman scattering, and a cross calibration between both methods was performed.

The scattered Rayleigh power, P_{Ray}, was obtained from the scattering signal from Ar gas at a known temperature, density, and pressure within the reactor. Regarding the absolute Ar pressure, we had to conclude from a systematic data analysis on all of our measurements that the actual absolute pressure during our measurements could have been somewhat higher. Therefore, the n_e could be higher by 10%–13% than what is reported in the present paper.

The Raman calibration method is similar to the one used by de Regt *et al.* [20] and van de Sande *et al.* [22]. The scattered Raman power, P_{RM}, was obtained from the fitting of the characteristic nitrogen Raman spectrum at a controlled pressure and temperature [26] and thus for a known gas density n_g. Similarly to the Thomson scattering signal, the Raman signal is accompanied by stray light and Rayleigh scattered light. In order to collect a high Raman intensity while avoiding blooming of the CCD detector the central part of the spectrum was blocked by a strip. This results in a spectrum like the one shown in Fig. 7, where about $100\,\mathrm{cm}^{-1}$ at the center is affected by the use of the strip. This area is excluded from the Raman fitting (open circles in the plot). Raman calibration has the advantage of having a wider spectrum and blocking the central part only disturbs a few Raman peaks close to the center, leaving enough peaks to perform an accurate fitting.

The scattered power of the Thomson signal P_{TS} is proportional to the electron density and the scattering cross section, in the same way as for the Raman and Rayleigh scattered

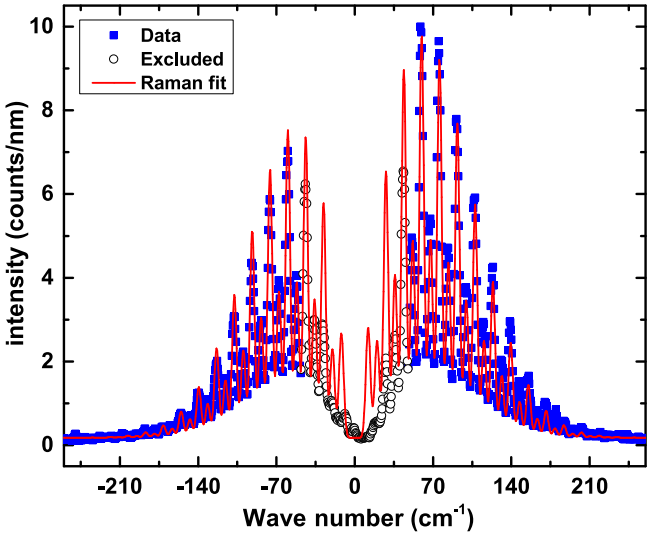

FIG. 7. Fitted Raman spectrum of nitrogen (normalized) used for the absolute calibration of the Thomson scattering signals. The spectral range blocked by the strip (see text for explanation) is from 530.6 to 533.4 nm. The background pressure is 5280 Pa, and the spectrum is obtained by integrating over 600 laser shots. The open circles correspond to the blocked part to avoid blooming of the detector.

powers. Taking the ratio of the Thomson and Rayleigh (or Raman) scattered powers we obtain the following equation:

$$\frac{P_{\mathrm{TS}}}{P_{\mathrm{Ray}}} = \frac{c\, n_e\ d\sigma_{\mathrm{TS}}/d\Omega}{c\, n_g\ d\sigma_{\mathrm{Ray}}/d\Omega}, \tag{1}$$

where c is a constant related to the spatial dimensions of the focused laser beam, which is assumed to be the same for both measurements. The ratio of the differential cross sections of Rayleigh (or Raman) scattering to Thomson scattering for argon is $\Gamma_{\mathrm{Ray}} = 6.80 \times 10^{-3}$ and for nitrogen in the case of Raman scattering is $\Gamma_{\mathrm{RM}} = 8.15 \times 10^{-5}$ [22] (at detection angle of 90°). After treating the Thomson measurements as outlined above, the total scattered power, P_{TS}, is obtained from the area of the Gaussian fit to the Thomson signal (see Fig. 6). The value of n_e is directly obtained from Eq. (1). T_e is obtained from the width at $1/e$ of the maximum intensity of the Thomson scattering spectrum. Comparing the electron densities from both methods we find a difference of less than 11%. We conclude that the results of both methods are in good agreement.

Rayleigh calibration is a well established technique [4,7,10], and due to the experimental conditions of the present work Rayleigh scattering was more suitable to perform. This because for Raman calibration nitrogen gas was used, which could lead to residual gas contamination during the Thomson measurements. Therefore, Rayleigh calibration was the method used to determine the electron density and temperature in all the measurements presented in this work.

The main sources of errors are statistical errors by fluctuations in the laser power and plasma conditions, errors induced by the calibration of the stray light subtraction process, and errors in the inaccuracy of the fitting. The overall error is less than 20%.

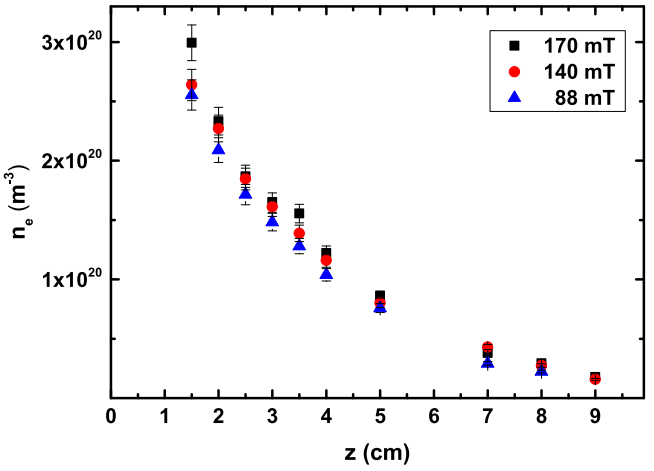

FIG. 8. Measured n_e along the expansion axis as a function of the distance from the exit of the nozzle, at three different magnetic field strengths: 88, 140, and 170 mT. The experimental conditions were H_2 flow of 3000 sccm, $p_{BG} = 88.3$ Pa, and $I_{arc} = 45$ A through the arc source. The statistical error was 5%.

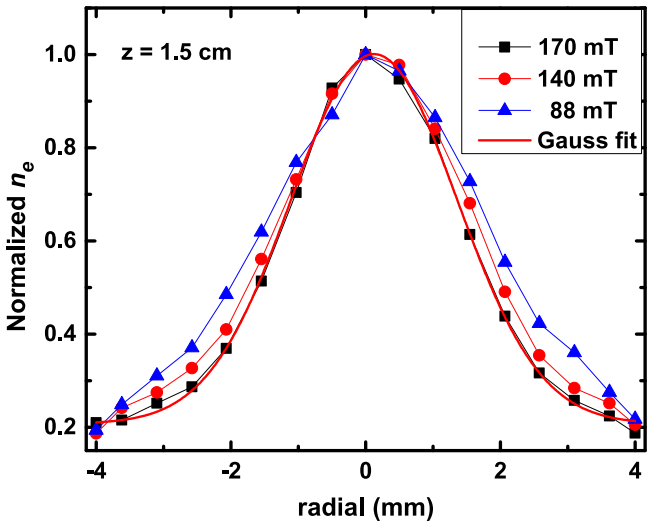

FIG. 9. Normalized n_e radial profiles at $z = 1.5$ cm. The experimental conditions were the following: H_2 flow of 3000 sccm, $p_{BG} = 88.3$ Pa, and $I_{arc} = 45$ A. The FWHMs of the fitted Gaussian profiles are 2.9, 3.2, and 3.7 mm for 170, 140, and 88 mT respectively.

IV. RESULTS

A. Thomson scattering measurements

1. Electron density as a function of magnetic field

Electron densities (n_e) along the main expansion axis, measured by Thomson scattering, are plotted in Fig. 8. Three different magnetic fields were used: 88, 140, and 170 mT. The experimental plasma conditions were filling pressure of 88.3 Pa, hydrogen flow of 3000 sccm, and a total current through the cathodes inside the cascaded arc of 45 A. The shortest distance from the nozzle exit at which the measurements were performed was $z = 1.5$ cm (see Sec. III A). In Fig. 8 we can observe that along the main expansion axis n_e decays from a maximum value of 3.0×10^{20} m^{-3} at $z = 1.5$ cm to a value of 1.7×10^{19} m^{-3} at $z = 9.0$ cm, almost independent of magnetic field strength. The statistical error on n_e was about 5%. This error was estimated in a series of 15 measurements under the same experimental conditions at the same position from the plasma source. Similarly the statistical error for T_e was determined to be about 7%.

Figure 9 shows the normalized radial electron density profiles of a hydrogen plasma for three magnetic fields at $z = 1.5$ cm from the arc nozzle. Narrowing of the n_e profile at the highest magnetic field strength can be observed, which means better plasma confinement. The n_e radial profiles exhibit a Gaussian shape. The full width at half maximum (FWHM) of the fitted Gaussian profiles are 2.9, 3.2, and 3.7 mm for 170, 140, and 88 mT, respectively.

2. Axial development of the electron temperature as a function of the magnetic field

Electron temperatures (T_e) plotted in Fig. 10 correspond to the same conditions as used for the measurements presented in Sec. IV A. For the two high-magnetic field cases, 140 and 170 mT, the values for T_e are similar and decay as a function of the distance from the exit of the nozzle almost in the same manner. For these two magnetic field strengths the maximum T_e is about 2.5 eV at $z = 1.5$ cm and decreases smoothly along the main axis, down to about 0.77 eV at $z = 9.0$ cm. At 88 mT the electron temperature along the expansion axis is lower than in the other two cases.

3. n_e and T_e as functions of plasma current at low downstream pressure

The electron density and temperature were determined for three different input arc currents: 45, 60, and 75 A, leading to three different input powers (7.1, 8.7, and 10.3 kW, respectively). During these measurements the gas flow was 3000 sccm, $p_{BG} = 9.8$ Pa, and a constant magnetic field strength of 88 mT was used. Figure 11 shows the local n_e

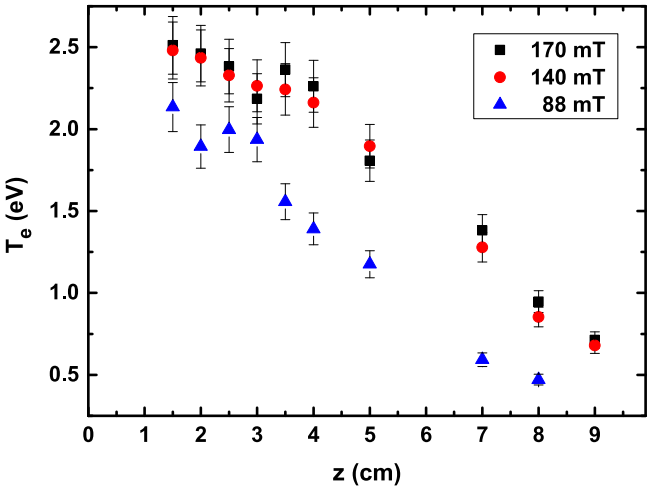

FIG. 10. Measured T_e along the expansion axis as a function of the distance from the exit of the nozzle, at three magnetic field strengths: 88, 140, and 170 mT. The experimental conditions were H_2 flow of 3000 sccm, $p_{BG} = 88.3$ Pa, and $I_{arc} = 45$ A. The statistical error is 7%.

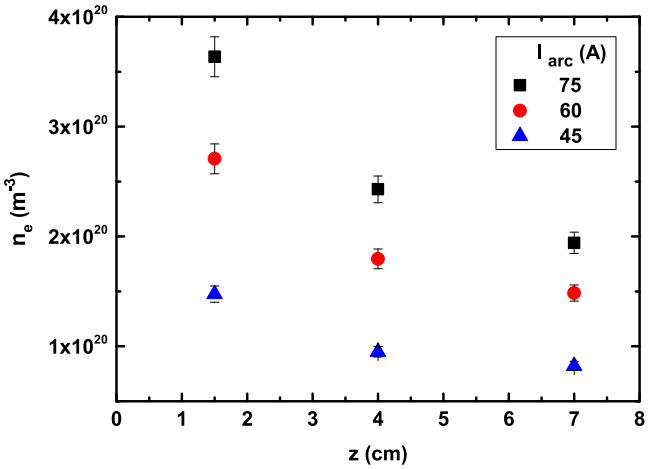

FIG. 11. Measured n_e along the expansion axis for three arc currents, i.e., 45, 60, and 75 A, and at three distances from the exit of the nozzle, i.e., 1.5, 4.0, and 7.0 cm. Experimental conditions were H_2 flow of 3000 sccm, $p_{BG} = 9.7$ Pa, and $B = 88$ mT.

measured on axis at three positions along the expansion axis: 1.5, 4.0, and 7.0 cm. The highest value of n_e, 3.6×10^{20} m^{-3}, was measured at an arc current of 75 A and at $z = 1.5$ cm. It can be seen that n_e decreases as a function of current and distance.

In Fig. 12 the electron temperature as a function of the distance from the exit of the arc for three different arc currents is shown. At 4.0 cm T_e shows a maximum for the three currents. Also, T_e increases at decreasing arc currents.

To elucidate whether T_e is inversely proportional to the input power, we performed a radial analysis at different z positions. For the position $z = 1.5$ cm, T_e radial profiles for arc currents of 45, 60, and 75 A are plotted in Fig. 13. For the other positions it was found that the measured electron temperature follows a trend very similar to that observed in Fig. 13.

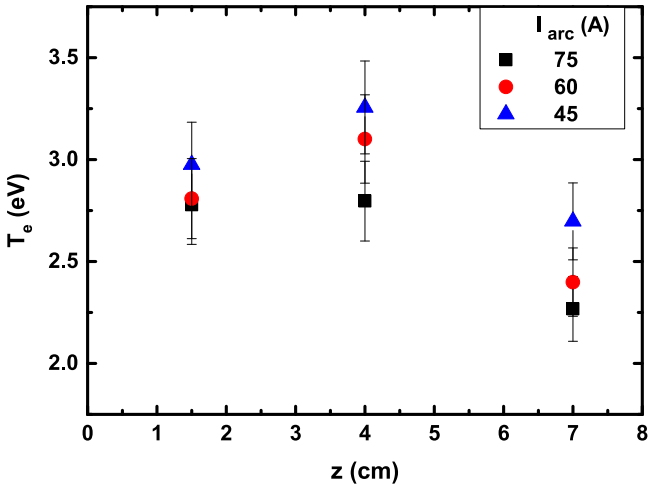

FIG. 12. Measured T_e along the expansion axis for three arc currents: 45, 60, and 75 A at $z = 1.5$, 4.0, and 7.0 cm. Experimental conditions were H_2 flow of 3000 sccm, $p_{BG} = 9.7$ Pa, and $B = 88$ mT.

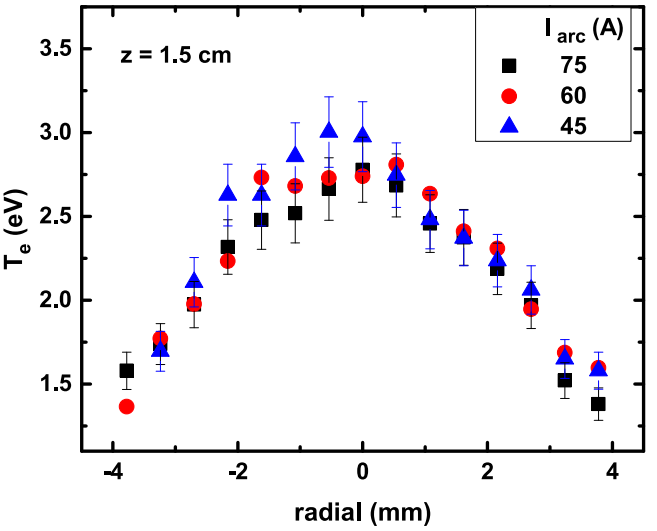

FIG. 13. Measured T_e radial profiles for the three arc currents: 45, 60, and 75 A at $z = 1.5$ cm. The experimental conditions were H_2 flow of 3000 sccm, $p_{BG} = 9.7$ Pa, and $B = 88$ mT.

From the plots it is evident that the radial profiles are similar in shape. A small difference is observed at the center of the radial profiles, but this is within the error bars.

V. DISCUSSION

In this section we present a general hypothesis that can provide a qualitative description of the trends observed for the electron densities and temperatures as a function of three main parameters: magnetic field strength, arc current, and background pressure. Magnetohydrodynamic effects due to the current through the plasma beam and the corresponding induced magnetic fields are discussed, as well as their relation with the Ohmic heating of the plasma. The influence of the background pressure on the plasma density, mainly due to molecular activated recombination (MAR) will also be treated.

A. Electron density behavior in the expanding plasma

1. *Effect of the arc current*

In this section we will discuss the effect of the arc current on n_e in the expanding plasma. A constant B field of 88 mT was applied to the plasma, while the arc current was increased as indicated in Sec. IV C. At higher arc currents the electron density increases because of the increase in power density. Excited hydrogen atoms (H^*) are present in the magnetized plasma. At sufficiently high electron densities these H^* are susceptible to being reionized leading to larger electron densities. This has been observed by Veremiyenko *et al.* [27] and Vijvers *et al.* [14] and confirmed by our measurements (see Fig. 11). It shows that with the arc current the electron density can be controlled.

2. *Effect of the B field*

The external magnetic field experienced by the expanding plasma induces a confinement of the charged particles, inducing a decreasing diffusion of n_e perpendicular to the

magnetic field lines. Electrons and ions under the action of the Lorentz force describe helical trajectories along the field lines giving rise to the gyrofrequency (in rad/s) [28],

$$\omega_{e,i} = \frac{eB}{m_{e,i}}, \tag{2}$$

where e is the elementary charge (in coulombs), B is the magnetic field strength (in teslas), and $m_{e,i}$ are the electron and ion masses (in kg), respectively. The Hall parameter for electrons and ions is obtained by taking the ratio between the gyro-frequency and collision frequency for, respectively, electron-ion υ_{ei} and ion-ion υ_{ii} collisions [9]:

$$H_{ei} = \frac{\omega_e}{\upsilon_{ei}} = 6.3 \times 10^{22} \frac{\hat{T}_e^{3/2}\, B}{n_e \ln(\Lambda)}, \tag{3}$$

$$H_{ii} = \frac{\omega_i}{\upsilon_{ii}} = 2.0 \times 10^{21} \frac{\hat{T}_i^{3/2}\, B}{A_i^{1/2}\, n_e \ln(\Lambda)}, \tag{4}$$

where $\hat{T}_e$ and $\hat{T}_i$ correspond to the electron and ion temperature (in eV), $\ln(\Lambda)$ is the Coulomb logarithm (under our experimental conditions in the range of 8.2–8.9), and A_i is the atomic mass number of the ion (in amu). If the Hall parameter is larger than 1, the charged particle is confined by the magnetic field lines; i.e., the charged particles describe a complete gyromotion around the magnetic field lines before undergoing a collision.

To show the connection between previous work done in our group by van Harskamp *et al.* [9] and the present work, we performed measurements close to the nozzle under experimental conditions similar to theirs. The background pressure, gas flow, and arc current were the same as used in [9]. Only a slightly higher B field (17 mT) than the B field of van Harskamp *et al.* (14 mT) had to be used, since that was the lowest B field at which we could determine n_e and T_e with our Thomson scattering setup.

The electron density and temperature measured using Thomson scattering at $z = 1.5$ cm and $B = 17$ mT were 5.8×10^{19} m^{-3} and 1.6 eV, respectively. Based on the densities of highly excited states recorded at the same position in the expansion, and assuming Saha equilibrium, van Harskamp calculated an electron density of 6.0×10^{19} m^{-3}. He deduced from a Fulcher-band analysis an electron temperature of 1.7 eV. This shows that our measurements using Thomson scattering and the calculations by van Harskamp are in good agreement. In Fig. 14 are shown the raw Thomson scattering signals (including the contributions of Rayleigh scattering and the stray light at the center of the spectrum). It can be seen that for B fields of 88 mT and higher, the Thomson signals are very similar, while for $B = 17$ mT there is a noticeable decrease of the signal, which means lower electron density and temperature.

Following the treatment by Vijvers *et al.* [14] in which parameters of the plasma in the source are predicted on the basis of mass and energy balances, we calculated n_e and T_e in our plasma source. For a B field of 17 mT the calculation leads to $n_e \approx 1.0 \times 10^{21}$ m^{-3} and $T_e \approx 2$ eV, then, the resulting Hall parameter is around 0.5. With increasing distance from the nozzle exit, the Hall parameter (in the plasma expansion) will rise to about 3–10, which is in agreement with the present observations. For the higher B fields, the plasma is at the exit of the arc magnetized. Under those conditions diffusion is limited. As a consequence, losses are smaller and thus plasma density is higher. For the low B field (17 mT) the plasma is not magnetized at the exit of the arc. This leads to an increased, ambipolar diffusion, resulting in a higher loss and thus a lower electron density.

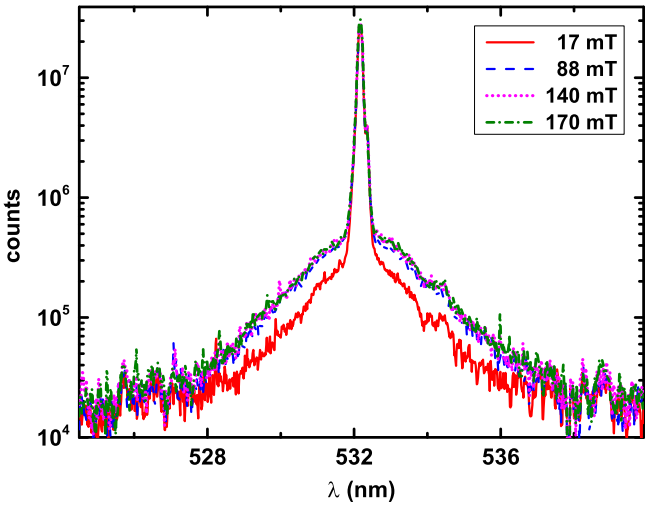

FIG. 14. Thomson and Rayleigh scattering and stray light signals of a hydrogen plasma at magnetic fields of 17, 88, 140, and 170 mT, and background pressure of 9.7 Pa.

At a background pressure of 88.3 Pa the Hall parameters for the electrons at B fields of 88, 140, and 170 mT are in the range of 8–33, indicating that the electrons are confined. On the other hand, the Hall parameters for the ions, under the same conditions, are between 0.05 and 0.2, indicating that the ions are not magnetically confined. However, since charge neutrality in the plasma has to be preserved, the ion diffusion will be hampered.

Since we are dealing with a magnetized plasma it is important to consider the effects of the induced currents and magnetic fields in the plasma. Just the presence of the plasma itself already modifies the magnetic field configuration. The axial plasma current $J_\parallel$ will induce a poloidal magnetic field B_θ, giving rise to an effective radial inward pinch force. At the border of the confined plasma this poloidal magnetic field can be approximated by $B_\theta = \mu_0\, I_0/2\pi\ r$, where r is the plasma radius and $I_0 \cong \int_0^R J_\parallel(r) 2\pi r\, dr$ $(R \leqslant r)$. Taking this into account the resultant total magnetic field is given by $B_{\mathrm{Tot}} = B_\parallel + B_\theta$. The values of the total magnetic field are shown in Table I. These values show that the contribution of the induced poloidal magnetic field B_θ is less than 5% of the applied 88 mT and lower than 3% for 140 and 170 mT.

3. *Effect of the background pressure*

The effect of the background pressure on n_e can be seen in Fig. 15 for two pressures, i.e., 9.7 and 88.3 Pa at a B field of 88 mT. The total current in the arc was 45 A. A faster decay of n_e at higher pressure was observed, indicating that the loss of charged particles becomes larger as the pressure

TABLE I. Measured values of T_e, plasma radius, and calculated values of Ohmic heating as a function of the applied magnetic field at $z = 1.5$ cm, $p_{BG} = 88.3$ Pa, and an arc current of 45 A.

B_{Tot} (mT)	r (m)	Q_{Ohmic} (W m^{-3})	T_e (eV)
92	1.8×10^{-3}	2.2×10^{9}	2.2
145	1.6×10^{-3}	3.5×10^{9}	2.46
176	1.4×10^{-3}	4.7×10^{9}	2.5

rises. This behavior can be explained by the effect of molecular activated recombination (MAR) [29,30], which increases with pressure and becomes anomalously fast at pressures around 100 Pa [10]. In the MAR process of hydrogen, first a molecular ion is produced via charge exchange between a hydrogen ion and a background gas molecule. Subsequently, dissociative recombination of an electron with the molecular ion, producing two hydrogen atoms, results in an efficient loss channel for electrons.

Under our gas flow and gas pump conditions the residence time is larger than the transit time of the plasma from the nozzle exit to the other end of the reactor [29]. This means that particles, mainly H_2, will recirculate several times before being pumped out of the reactor. The presence of recirculation zones, formed between the plasma beam and the walls of the reactor, has been reported previously [10]. These recirculating particles (mainly H_2) contribute to the interaction between background gas and plasma. Since at higher pressure more particles diffuse into the plasma expansion a higher pressure will lead to a faster decay of the electron density.

4. Stationary shock and background pressure

A characteristic of expanding plasmas is the formation of a stationary shock front [29–32]. The position z_M of this front is determined by

$$z_M = 1.8 \times 10^{-2} \sqrt{\frac{\Phi}{p_{BG}}} \sqrt[4]{A\, T_s}, \tag{5}$$

in which Φ is the gas flow in standard cubic centimeters per second (sccs), p_{BG} is the background pressure in Pa, A is the atomic mass number, and T_s corresponds to the source temperature at the axis in eV. The shock position at a pressure of 88.3 Pa is about 1.5 cm from the exit of the arc. Due to the experimental conditions our closest measurement point with respect to the exit of the arc was 1.5 cm (see Sec. III A). Hence, for the high-pressure case the plasma is already subsonic at $z_M > 1.5$ cm. For the low-pressure case, i.e., at $p_{BG} = 9.7$ Pa, the shock front is expected further downstream in the expansion at $z_M \cong 5$ cm. In Fig. 15 it can be observed that in the first centimeters of the expansion, on axis the electron density at 88.3 Pa is higher than at 9.7 Pa. This is in agreement with the trends reported by van de Sanden *et al.* [2,3,29], who measured electron densities in argon expanding plasmas at different background pressures.

They show that for different pressures, n_e decreases in the supersonic domain and increases after the shock front. And since the position of the shock front depends on the pressure, close to the source, at the same position but at different pressures, different n_e can be measured, as has been shown in [2,3,29].

However, after $z = 4$ cm at 9.7 Pa the decrease in n_e is slower with respect to the 88.3 Pa case. At lower pressure less H_2 is present in the background, and thus fewer MAR processes take place (see Fig. 15). de Graaf *et al.* [10] reported anomalous fast recombination in a hydrogen expanding plasma already at a pressure about 50 Pa. They proposed the existence of a molecular channel based on the conversion of atomic to molecular ions by charge transfer. Veremiyenko *et al.* [27] have shown that the expanding plasma becomes narrower when the background pressure is increased; i.e., the plasma beam is constrained by the recirculating background particles, inducing faster recombination. The comparison of n_e at two different background pressures allows observing that after $z = 4$ cm at $p_{BG} = 88.3$ Pa, the decay of n_e along the main expansion axis occurs faster with respect to the $p_{BG} = 9.7$ Pa case (see Fig. 15).

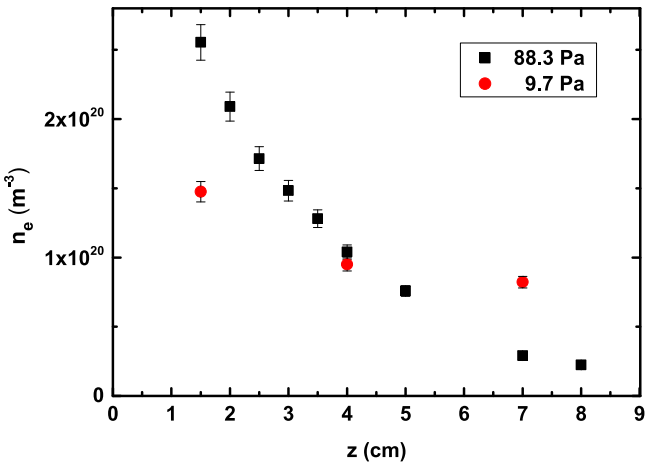

FIG. 15. Electron density in a hydrogen plasma as a function of the distance from the exit of the source for two different background pressures. Both measurements were performed at an H_2 flow of 3000 sccm, $I_{arc} = 45$ A, and $B = 88$ mT, and background pressures $p_{BG} = 9.7$ Pa and $p_{BG} = 88.3$ Pa.

B. Electron temperature behavior in the expanding plasma

In Figs. 10, 12, and 13 the electron temperature as a function of the distance from the exit of the arc as well as radial measurements have been shown for different magnetic field strengths and arc currents. The electron temperature close to the exit of the nozzle has also been determined previously in two different ways by others. van Harskamp [23] used the emission of the Fulcher band of the hydrogen molecule ($d^3\Pi_u - a^3\Sigma_g^+$) to determine T_e. They found an electron temperature of around 2 eV on the axis of the expansion close to the exit of the nozzle at similar background pressure and arc current, but at a slightly lower magnetic field strength (14 mT instead of 17 mT, used in our work). Schram *et al.* have

shown that T_e close to the nozzle exit can be calculated by

$$T_e = \frac{E_{\text{ion}}}{\ln(10\ S\ \sqrt{A}) - \ln(T)}, \tag{6}$$

where E_{ion} is the ionization energy of the H atom (13.6 eV), and S is the product of the pressure times the characteristic length ($\approx 1 \times 10^{-3}$ m) [30] of a high-density and -temperature plasma at the exit of the source, applicable in our case. Here A is the mass number and $T = 0.17$ eV is the heavy particle temperature taken from van Harskamp *et al.* [23]. Using the previous conditions Eq. (6) [23] yields an electron temperature of about 2.7 eV at the exit of the nozzle, which is in good agreement with our measurements (≈ 2.5 eV) at the vicinity of the exit nozzle.

In Fig. 12 the electron temperature at three different positions on the expansion axis shows a decrease at increasing arc currents. In Fig. 13 are shown the corresponding T_e radial profiles for the three used arc currents at $z = 1.5$ cm. A higher T_e at a lower arc current could be related to the energy transfer time in collisions of electrons and ions. The energy transfer time is inversely proportional to the collision frequency between electrons and ions, ν_{ei}, which is given by $\nu_{ei} = n_i \sigma_{ei} v_e$. Hence, at higher arc currents under the same conditions of pressure and B field, there is a higher n_e, and therefore higher n_i. The energy transfer time is shorter at higher arc currents resulting in a faster thermalization of the plasma, i.e., faster cooling of the electrons at high arc currents. It was found that despite the small deviation at the on-axis values, the T_e profiles overlap on the sides; i.e., the radial T_e profiles remain almost constant at different arc currents. At $z = 4.0$ cm T_e rises for the three arc currents. This could be related to the fact that a shock front, mainly composed by neutrals, is expected to be formed around $z = 5$ cm [see Eq. (5)] for a hydrogen flow of 3000 sccm and $p_{\text{BG}} = 9.7$ Pa. A rarefied zone is formed before the shock front, which results in the decrease of the particle density, mainly of neutrals. On the other hand, according to the formalism of the Langevin equation, the electron-neutral collisions decrease exponentially the average electron velocity (i.e., T_e), at a rate of the collision frequency between electrons and neutrals [28]. Hence, the lower neutral density before the shock will result in less electron-neutral collisions, which could lead to the increase of T_e.

1. *Effect of pressure and B field*

In Fig. 16 the electron temperature as a function of distance from the exit of the arc is shown for a magnetic field of 88 mT and an arc current of 45 A, measured for two different pressures: 9.7 and 88.3 Pa. It can be seen that at 9.7 Pa the electron temperature first rises and then drops, while at 88.3 Pa T_e decreases from the first measurement position at $z = 1.5$ cm. Something to consider is that at high pressure the presence of more H_2 which diffuses into the plasma will lead to plasma cooling. At lower pressures not only the electron density in the expansion is lower but also the neutral density is lower ($\sim 9 \times 10^{20}$ m^{-3}). This neutral density was measured under similar experimental conditions by Mazouffre *et al.* [33], Vankan *et al.* [17], and van de Sanden *et al.* [29]. At higher pressures the neutral density in the plasma expansion is higher

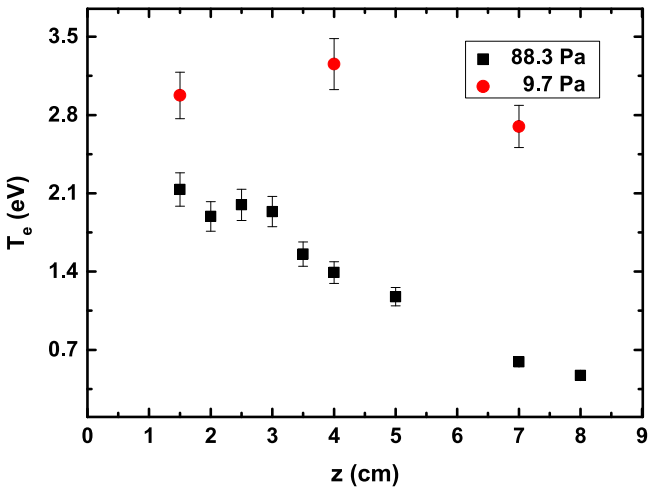

FIG. 16. Measured T_e as a function of the distance to the exit of the nozzle of a magnetized hydrogen plasma at a $p_{\text{BG}} = 9.7$ Pa and $p_{\text{BG}} = 88.3$ Pa. Both measurements were performed for an H_2 flow of 3000 sccm, $I_{\text{arc}} = 45$ A, and $B = 88$ mT.

and hence in the source a lower T_e suffices to ensure enough ionization.

An explanation of the T_e behavior as a function of the applied magnetic field can be found by considering the effect of Ohmic heating in the plasma expansion. When the plasma is confined by a magnetic field the mobility of the charged particles is constrained mainly to the expansion axis (z axis) which is in the same direction as the applied B field. As a consequence the current flows along the magnetic field lines. The current penetration length and the Ohmic heating depend on the magnetic field strength. For a better magnetic confinement, there is a higher current penetration which leads to an increase in the plasma heating. This plasma heating can be linked to the relatively high T_e for the more confined plasma at higher magnetic fields. The Ohmic heating Q_{Ohmic} is defined as

$$Q_{\text{Ohmic}} = \sigma_{\parallel}\ E_z^2, \tag{7}$$

where $\boldsymbol{E}_z$ is the electric field along the z axis and $\sigma_{\parallel}$ is the Spitzer conductivity. By the generalized Ohm's law the axial electric field $\boldsymbol{E}_z$ is related to the current density $\boldsymbol{j}(z)$ through $\boldsymbol{E}_z = \eta_{\parallel} \boldsymbol{j}(z)$, where $\eta_{\parallel} = 1/\sigma_{\parallel}$ is the plasma resistivity and $\boldsymbol{j}(z) = \boldsymbol{I}_{\text{arc}}/\pi r^2$. Here we take the radius r equal to the FWHM obtained from the measured radial profiles of the plasma beam confined at different B fields (see Fig. 9). Notice that the dependence of Q_{Ohmic} on the plasma radius is r^4, stressing the relevance of the magnetic confinement. Finally we can calculate the Ohmic heating for the cases under study (see Table I).

The values in Table I show that Q_{Ohmic} increase for smaller plasma radius and that the values obtained for the Ohmic heating are consistent with the measured T_e (see Fig. 10); i.e., the increment in Q_{Ohmic} leads to the rise of T_e. Although calculations on the heating do not give a direct value of the temperature, it is an initial and reasonable explanation that a higher Q_{Ohmic} is related to a higher T_e.

VI. CONCLUSIONS

Thomson scattering was successfully applied to determine n_e and T_e in a magnetized H_2 expanding thermal plasma for different parameters, such as magnetic field, arc current, and background pressure. The maximum n_e measured as a function of the magnetic field was $3.0 \times 10^{20}\,\mathrm{m}^{-3}$, at $z = 1.5\,\mathrm{cm}$. The electron density along the z axis decays exponentially and appears not to be susceptible to a change of magnetic field in the range of 88–170 mT. It can be said that in the plasma source at the lowest field the electrons are not magnetized. This leads to more losses, resulting in a lower density. The corresponding T_e shows an increase for higher magnetic fields. We propose Ohmic heating as a mechanism leading to the increase of T_e. We show that for a better confined plasma, Ohmic heating increases, which leads to a higher T_e.

Higher arc currents lead to an increase in the electron density, reaching up to $3.6 \times 10^{20}\ \mathrm{m}^{-3}$ and, decaying as a function of distance from the nozzle exit along the center of the plasma beam. The electron temperature reaches values up to 3.2 eV at the lowest arc current and lowest back ground pressure. The arc current in combination with the magnetic confinement are key parameters to induce higher n_e in the plasma.

Higher background pressures lead to a faster decay of the electron density in the plasma expansion, which is in agreement with the trends reported in other works. But after $z = 4.0\,\mathrm{cm}$ n_e at low pressure becomes about a factor of 2 higher in the downstream plasma ($z = 7\,\mathrm{cm}$). The presence of the shock front appears to be related to the rise in electron temperature at $z = 4.0$ cm, at the low pressure of 9.7 Pa. This can be attributed to the anomalous fast recombination as mentioned in this work. The observed decrease on T_e at high pressure is ascribed to the presence of more background H_2 molecules which diffuse into the plasma beam leading to cooling of the plasma, and therefore to lower T_e. The radial T_e profiles as a function of the arc current appear to be almost constant, especially on the flanks of the profiles.

ACKNOWLEDGMENTS

This work is supported by NanoNextNL, a micro and nanotechnology consortium of the Government of Netherlands and 130 partners. We greatly appreciate the skillful technical assistance of M. J. F. van de Sande, H. M. M. de Jong, J. J. A. Zeebregts, and J. J. L. M. Meulendijks. We also like to acknowledge H. J. van der Meiden for his assistance during the construction of the Thomson scattering diagnostic and Thomson scattering fitting program, B. L. M. Klarenaar for the use of his Raman fitting program, and Prof. T. Gans from the University of York for lending us his iCCD detector.

[1] G. M. W. Kroesen, D. C. Schram, A. T. M. Wilbers, and G. J. Meeusen, Contrib. Plasma Phys. **31**, 27 (1991).
[2] M. C. M. van de Sanden, G. M. Janssen, J. M. de Regt, D. C. Schram, J. A. M. van der Mullen, and B. van der Sijde, Rev. Sci. Instrum. **63**, 3369 (1992).
[3] M. C. M. van de Sanden, J. M. de Regt, and D. C. Schram, Phys. Rev. E **47**, 2792 (1993).
[4] R. Engeln, K. G. Y. Letourneur, M. G. H. Boogaarts, M. C. M. van de Sanden, and D. C. Schram, Chem. Phys. Lett. **310**, 405 (1999).
[5] S. Mazouffre, M. G. H. Boogaarts, I. S. J. Bakker, P. Vankan, R. Engeln, and D. C. Schram, Phys. Rev. E **64**, 016411 (2001).
[6] P. Vankan, D. C. Schram, and R. Engeln, Chem. Phys. Lett. **121**, 400 (2004).
[7] O. Gabriel, P. G. J. Colsters, D. C. Schram, and R. Engeln, Plasma Sources Sci. Technol. **17**, 015011 (2008).
[8] H. Maecker, Z. Naturforsch., A: Astrophys. Phys. Phys. Chem. **11a**, 457 (1956).
[9] W. E. N. van Harskamp, C. M. Brouwer, D. C. Schram, M. C. M. van de Sanden, and R. Engeln, Phys. Rev. E **83**, 036412 (2011).
[10] M. J. de Graaf, R. Severens, R. P. Dahiya, M. C. M. van de Sanden, and D. C. Schram, Phys. Rev. E **48**, 2098 (1993).
[11] D. M. Goebel, G. Campbell, and R. W. Conn, J. Nucl. Mater. **121**, 277 (1984).
[12] N. Ohno, D. Nishijima, S. Takamura, Y. Uesugi, M. Motoyama, N. Hattori, H. Arakawa, N. Ezumi, S. Krasheninnikov, A. Pigarov, and U. Wenzel, Nucl. Fusion **41**, 1055 (2001).
[13] H. J. van der Meiden, Plasma Phys. Controlled Fusion **52**, 045009 (2010).
[14] W. A. J. Vijvers, C. A. J. van Gils, W. J. Goedheer, H. J. van der Meiden, D. C. Schram, V. P. Veremiyenko, J. Westerhout, N. J. L. Cardozo, and G. J. van Rooij, Phys. Plasmas **15**, 093507 (2008).
[15] G. J. van Rooij, H. J. van der Meiden, W. R. Koppers, A. E. Shumack, W. A. J. Vijvers, J. Westerhout, G. M. Wright, and J. Rapp, Plasma Phys. Controlled Fusion **51**, 124037 (2009).
[16] G. De Temmerman, M. A. van den Berg, J. Scholten, A. Lof, H. J. van der Meiden, H. J. N. van Eck, T. W. Morgan, T. M. de Kruijf, P. A. Zeijlmans van Emmichoven, and J. J. Zielinski, Fusion Eng. Des. **88**, 483 (2013).
[17] P. Vankan, D. C. Schram, and R. Engeln, Plasma Sources Sci. Technol. **14**, 744 (2005).
[18] O. Gabriel, D. C. Schram, and R. Engeln, Phys. Rev. E **78**, 016407 (2008).
[19] H. J. van der Meiden, A. R. Lof, M. A. van den Berg, S. Brons, A. J. H. Donné, H. J. N. van Eck, P. M. J. Koelman, W. R. Koppers, O. G. Kruijt, N. N. Naumenko *et al.*, Rev. Sci. Instrum. **83**, 123505 (2012).
[20] J. M. de Regt, R. A. H. Engeln, F. P. J. de Grote, J. A. M. van der Mullen, and D. C. Schram, Rev. Sci. Instrum. **66**, 3228 (1995).
[21] A. F. H. van Gessel, E. A. D. Carbone, P. J. Bruggeman, and J. A. M. van der Mullen, Plasma Sources Sci. Technol. **21**, 015003 (2012).
[22] M. J. van de Sande and J. A. M. van der Mullen, J. Phys. D: Appl. Phys. **35**, 1381 (2002).

[23] W. E. N. van Harskamp, Ph.D. thesis, Eindhoven University of Technology, 2012. Available online at https://pure.tue.nl/ws/files/3541841/735309.pdf.

[24] H. J. van der Meiden, Ph.D. thesis, Eindhoven University of Technology, 2011. Available online at https://pure.tue.nl/ws/files/3080010/694404.pdf.

[25] H. J. Kunze, in *Plasma Diagnostics*, edited by W. Lochte-Holtgreven (North-Holland Publishing, Amsterdam, 1968).

[26] B. L. M. Klarenaar, M.Sc. thesis, Eindhoven University of Technology, 2014. Available online at http://alexandria.tue.nl/extra2/afstversl/n/Klarenaar_2014.pdf.

[27] V. P. Veremiyenko, Ph.D. thesis, Eindhoven University of Technology, 2006. Available online at https://pure.tue.nl/ws/files/1682104/200610969.pdf.

[28] J. A. Bittencourt, *Fundamentals of Plasma Physics*, 3rd ed. (Springer, New York, 2004).

[29] M. C. M. van de Sanden, J. M. de Regt, and D. C. Schram, Plasma Sources Sci. Technol. **3**, 501 (1994).

[30] D. C. Schram, S. Mazouffre, R. Engeln, and M. C. M. van de Sanden, in *Atomic and Molecular Beams: The State of the Art 2000*, edited by R. Campargue (Springer, NewYork, 2001).

[31] W. S. Young, Phys. Fluids **18**, 1421 (1975).

[32] H. Ashkenas and F. S. Sherman, in *Proceedings of Fourth International Symposium on Rarefied Gas Dynamics*, *Toronto* (1964).

[33] S. Mazouffre, P. Vankan, R. Engeln, and D. C. Schram, Phys. Plasmas **8**, 3824 (2001).